Mechanical Systems and Signal Processing 164 (2022) 108262

Contents lists available at ScienceDirect

Mechanical Systems and Signal Processing

journal homepage: www.elsevier.com/locate/ymssp

A machine learning approach for maximizing direct current power of nonlinear energy harvesting systems subjected to periodic impulse excitation

Wen Cai [a], Ryan L. Harne [b,*]

[a] Department of Mechanical and Aerospace Engineering, The Ohio State University, Columbus, OH 43210, USA
[b] Department of Mechanical Engineering, The Pennsylvania State University, University Park, PA 16802, USA

ARTICLE INFO

Keywords:
Nonlinear energy harvesting systems
Periodic impulse excitation
Physics-guided
Machine learning algorithms
Dynamic regimes
Optimal DC power delivery

ABSTRACT

Vibration energy harvesting is a thoroughly tested approach to support the growing number of Internet-of-Things devices by providing a local and sustainable electrical power resource. Yet, the discovery of best practices for deploying vibration energy harvesters in environments is limited by inability to decipher high-dimensional data associated with design and implementation details. The study aims to devise one such approach to conclusively identify conditions under which an impulse-excited nonlinear energy harvesting system delivers peak electrical power. To accomplish this goal, physics-based and machine learning algorithms are integrated to uncover the underlying relationships between the impulse-induced nonlinear dynamics and the result converted electrical energy. The accuracy of the predictions from a machine learning model are confirmed through experiments and against cross-validation simulation data. The parameters that result in snap-through, as determined through machine learning methods, are then probed through a first-principles model to confirm that optimal circuit design conditions agree with the principle of impedance matching. The findings guide attention to previously unseen nuances of exploiting nonlinear vibration energy harvesting systems in impulse excitation environments by revealing parameter sensitivities that inhibit or promote the realization of snap-through vibration for peak power generation. This research demonstrates a successful synthesis of machine learning algorithms and first principles models to guide attention to optimal designs of nonlinear energy harvesting systems subjected to periodic impulse excitation.

1. Introduction

With the ever-growing number of Internet-of-Things (IoT) devices to a trillion by 2025 [29], energy management becomes more of a challenge as conventional chemical batteries have a limited lifespan and undesirable service requirement. Compared with batteries, vibration energy harvesting is a promising option to provide sustainable power from the kinetic energy sources readily available in daily life, such as from human motion, vehicle wheel rotation, bridge vibration, and more [42].

Piezoelectric beams are widely utilized to transfer this kinetic energy to electrical power due to the high-power density of piezoelectric material [15]. Considering the broadband frequency nature that real vibration displays, nonlinearity such as bistability

* Corresponding author.
E-mail address: ryanharne@psu.edu (R.L. Harne).

https://doi.org/10.1016/j.ymssp.2021.108262
Received 27 January 2021; Received in revised form 14 May 2021; Accepted 19 July 2021
Available online 5 August 2021

has been introduced to maximize the harvested power in a wide frequency spectrum [39,38,16,13]. Cottone et al. [8] indicated a potential increase of 400% to 600% in harvesting alternate current (AC) power with bistable configuration when subjected to wide-spectrum stochastic excitation. Three possible vibration classes may be generated in bistable structures, including snap-through vibration with displacement crossing the two equilibria, intrawell vibration that oscillates around one equilibrium configuration, and chaotic vibration [13]. Recently, researchers have explored methods to attain high-energy snap-through vibration [3,4,45,25], such as activated potential energy profiles [46], and load perturbations [34]. In addition, since direct current (DC) power is required to power IoT sensors, nonlinear circuits are investigated when coupled with nonlinear energy harvesters to examine strategies that optimize harvested DC power [9,36,21]. Huguet et al. [19] explored the integration of bistable energy harvesters with synchronized electric charge extraction (SECE) circuits and found an increase in electric power and decrease in frequency bandwidth when subjected to harmonic excitation. Cai and Harne [3,4] proposed an analytical approach to determine optimal working conditions for buck-boost converters interfaced with nonlinear energy harvesters under pure harmonic excitation.

From this survey of state-of-art studies, pure harmonic or stochastic excitation is frequently examined to characterize and optimize the nonlinear dynamics of circuit-harvester integrations for sustainable electric power. Yet, the environment that energy harvesters are likely deployed within may experience complex excitation conditions, for instance impulse excitation induced by human motion, transportation, or other activities [40,27,31]. Harne et al. [18] constructed an analytical model with the Jacobian elliptic functions to predict transient electrodynamic behaviors of a bistable energy harvester interfaced with a resistive electric load. Due to the complexity of the Jacobian elliptic functions, the analytical model does not significantly ease the efforts to identify impulse-induced nonlinear dynamics except single impulse events [18,43]. Instead, numerical methods are widely employed to characterize other impulse-induced responses [30,14]. Quinn et al. [28] numerically identified improvements in harvested AC power and frequency response for periodically impulse-excited nonlinear energy harvesters. Further, Fang et al. [12] designed an asymmetric plucking-based bistable energy harvester to capture rotational energy by the impulsive event of contact.

While notable advancements have been achieved to integrate nonlinear circuits with nonlinear energy harvesters when the ambient excitations are harmonic or stochastic [9,36,21], to the best of the authors' knowledge the interactions among nonlinearities in the harvesting circuits and structures have not been characterized under periodic impulse excitation. Since many impulse-induced vibrations are more repetitive than singular events [40,27,31], prior modeling frameworks assume singular impulses on nonlinear energy harvesters do not apply [18,43]. In addition, researchers [7] have shown that parameters such as impulse magnitude, electromechanical coupling, and viscous damping directly affect the class of vibration that nonlinear energy harvesters may achieve, although only snap-through vibration is desirable for appreciable power generation [17]. Unfortunately, numerical methods are inefficient for the purpose of ad-hoc design optimization since the number of parameters is large, the nonlinearities and dynamics are non-smooth, and periodicity of energy harvester response may not occur in the same time scale as the impulse excitation [7]. Therefore, there remains a need for a unified model that comprehensively characterizes the dynamic mechanisms underlying optimized electrical power extraction from nonlinear energy harvesting systems subjected to periodic impulses.

Recent studies have formulated insightful physics-based understanding by harnessing advances in machine learning, especially when theoretical models are extremely challenging to formulate and machine learning methods alone cloud the underlying physics [20,41,33]. Brunton et al. [2] identified the governing equations for nonlinear dynamical systems by leveraging sparsity-promoting techniques and machine learning algorithms, demonstrating the ability of such an approach to uncover the salient system dynamics without a requisite theoretical method for guidance. Advancing this concept, Zhang and Sun [44] proposed a physics-guided neural network that employed a loss function to reduce the discrepancy between the neural network model outputs and finite element results. The numerical and experimental validations indicated the strength of the method in improving the generality and scientific consistency of damage detection. Due to the invariance of many systems in fluid dynamics, mechanics, and system dynamics, Ling et al. [23] developed an empirical model by incorporating the invariance properties of simulation data with machine learning processes to demonstrate direct accounting for system symmetries and scalability in the machine learning predictions that are consistent with the underlying physical relations. These examples highlight how emerging advances in data science are accelerating discovery and physical understanding of new problems across disciplines and suggest the broad applicability of such methods to engineering and science.

Inspired by these recent developments and considering the need to illuminate the multiphysics dynamic behaviors of impulse-excited nonlinear energy harvesting systems, this research creates an integrative theoretical and machine learning model for optimizing direct current power of nonlinear energy harvesting systems under periodic impulse excitation. Therefore, in the following section a theoretical model of a nonlinear energy harvester subjected to periodic impulses is introduced to study the system dynamics. Following experimental validation of the model, a machine learning approach is described to map the theoretical relations to discrete, non-smooth system dynamics each inducing distinct energy harvesting potential. The integrated machine learning and theoretical models are then explored to characterize dynamic regimes of snap-through vibration and provide guidance for best electrical power extraction. Finally, a summary of key findings is presented to conclude the report.

2. Nonlinear energy harvesters with magnetic coupling under periodic impulse excitation

2.1. Model for nonlinear energy harvester considering magnet rotation

A piezoelectric beam with additional magnetic potentials is frequently employed to construct a post-buckled energy harvesting system due to the ease of assembly and tuning [10]. Fig. 1(a) presents one approach to introduce magnetic coupling. In the schematic, a pair of repulsive magnets are employed, one of which is attached to the piezoelectric beam tip with a magnet holder. The position of

the other magnet holder is attached to the base, yet remains adjustable in location to regulate the nonlinearities acting on the system by magnetic repulsion. The tip mass M_0 at the free tip of the beam is constructed by magnet 1 and the magnet holder. A standard rectification circuit is connected to the piezoelectric beam to ensure a DC power delivery, Fig. 1(a).

For the nonlinear energy harvesting system shown in Fig. 1(a), the base (shown in light grey shade) is periodically impulsed, which moves the cantilever beam as well as the holder for magnet 2. In the following investigations, the higher order modes of the cantilever occur at sufficiently high frequencies to not contribute substantially to the dynamic examined here, corresponding to the fundamental excitation frequencies and sub-/superharmonics. The governing equation for the system is given in Eq. (1).

$$m\ddot{x}_L + c\dot{x}_L + k_1 x_L + k_3 x_L^3 + \alpha \mathrm{v_p} = \mathrm{F_{21}} \tag{1a}$$

$$C_p \dot{v}_p + i_p = \alpha \dot{\mathrm{x}}_\mathrm{L} \tag{1b}$$

$$i_p(t) = \begin{cases} C_r \dot{v}_r + \dfrac{v_r}{R};\ \text{if } v_p = v_r \\ -C_r \dot{v}_r - \dfrac{v_r}{R};\ \text{if } v_p = -v_r \\ 0;\ \text{if } |v_p| < v_r \end{cases} \tag{1c}$$

In Eq. (1), x_L is the beam tip displacement related to the fundamental mode; m, c, k_1, and k_3 are the equivalent mass, viscous damping, linear stiffness, and nonlinear stiffness due to the large deflection corresponding to the first vibration mode; α is the electromechanical coupling constant; C_p and C_r are respectively the internal capacitance of the piezoelectric beam and smoothing capacitance; v_p and v_r are respectively the voltage across the piezoelectric beam electrodes and rectified voltage; R relates to the resistance outside of the rectification bridge; i_p corresponds to the current passing into the rectification circuit; F_{21} is the magnetic force between magnets 1 and 2; The overdot operator indicates differentiation with respect to time t.

Before the application of impulse, the beam is assumed to rest at the static equilibrium position x^* The voltages are across the piezoelectric beam and rectifier are both zero. The initial conditions are given in Eq. (2a–d).

$$x_L|_{t=0^-} = x^*;\ \dot{x}_L\Big|_{t=0^-} = 0;\ v_p|_{t=0^-} = 0;\ v_r|_{t=0^-} = 0; \tag{2a–d}$$

Hereafter, the superscript '-' on time indicates the instant before applying the impulse, while the superscript '+' indicates the moment after impulse application.

The periodic impulse excitation applied in the study is assumed to be ideal as shown in Fig. 1(b). According to the impulse-momentum theorem, the velocity change is chosen to reflect the impulse applied. Therefore, the state changes caused by the periodic impulse excitation are given in Eq. (3a–d).

$$x_L|_{t=nT^+} = x_L|_{t=nT^-};\ \dot{x}_L\Big|_{t=nT^+} = \dot{x}_L\Big|_{t=nT^-} + I;\ v_p|_{t=nT^+} = v_p|_{t=nT^-};\ v_r|_{t=nT^+} = v_r|_{t=nT^-};\quad n = 0, 1, 2, 3 \cdots \tag{3}$$

The T is the period of the impulse excitation as shown in Fig. 1(b), n is the number of the impulse cycle that has been applied, and the absolute value of I indicates the magnitude of the impulse exerted to the system. Given the coordinate defined in Fig. 1(c), the positive value of I represents the impulse applied in the positive direction of the x axis, and the negative value of I suggests the impulse applied in the negative direction.

Since large amplitude vibration is preferred for nonlinear vibration energy harvesting systems, the magnet rotation is necessary to be examined since it determines the nonlinear force acting on the piezoelectric beam tip. For a clamped beam with attached tip-mass, the fundamental mode shape is approximated by

$$W_1(x) = C_4\left[(sin\beta_1 x - sinh\beta_1 x) - \frac{sin\beta_1 l + sinh\beta_1 l}{cos\beta_1 l + cosh\beta_1 l}(cos\beta_1 x - cosh\beta_1 x)\right] \tag{4}$$

where β_1 corresponds to the first eigenvalue determined by the characteristic equation shown in Eq. (5).

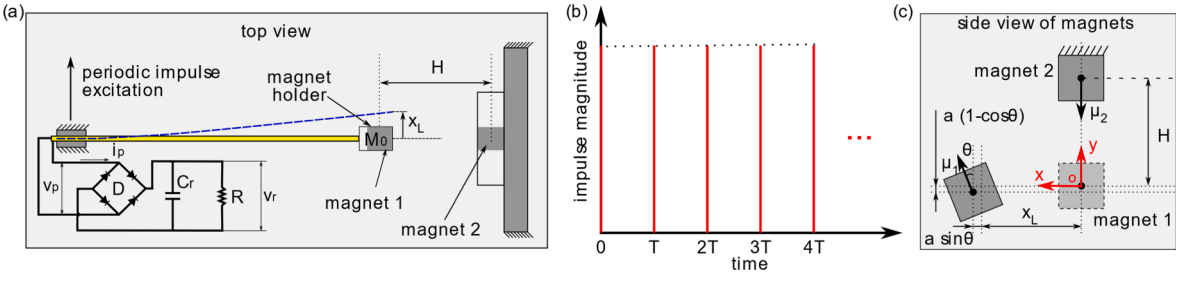

Fig. 1. (a) Schematic of nonlinear energy harvester connecting with standard rectification circuit. (b) Periodic impulse excitation. (c) Detailed schematic of repulsive magnets interaction.

$$1+\frac{1}{cos\beta_n l cosh\beta_n l}-R\beta_n l(tan\beta_n l-tanh\beta_n l)=0 \tag{5}$$

In Eq. (5), $R=\frac{M_0}{\rho A l}$ is a tip mass ratio; ρ and A are the equivalent density and cross section area of beam; and l is the beam length.

Normalizing the mode shape such that the beam tip displacement magnitude is equal to one, the coefficient C_4 is determined as shown in Eq. (6).

$$C_4=\frac{1}{(sin\beta_1 l-sinh\beta_1 l)-(sin\beta_1 l+sinh\beta_1 l)\,(cos\beta_1 l-cosh\beta_1 l)/(cos\beta_1 l+cosh\beta_1 l)} \tag{6}$$

Therefore, the rotation angle for the first order model shape is

$$W_1^{'}(x)=C_4\left[\beta_1(cos\beta_1 x-cosh\beta_1 x)-\frac{sin\beta_1 l+sinh\beta_1 l}{cos\beta_1 l+cosh\beta_1 l}\beta_1(-sin\beta_1 x-sinh\beta_1 x)\right] \tag{7}$$

The rotational angle at the beam free tip is then achieved by Eq. (8).

$$\theta=W_1^{'}(l)=\frac{(cos\beta_1 l-cosh\beta_1 l)-\frac{sin\beta_1 l+sinh\beta_1 l}{cos\beta_1 l+cosh\beta_1 l}(-sin\beta_1 l-sinh\beta_1 l)}{(sin\beta_1 l-sinh\beta_1 l)-\frac{sin\beta_1 l+sinh\beta_1 l}{cos\beta_1 l+cosh\beta_1 l}(cos\beta_1 l-cosh\beta_1 l)}\beta_1 x_L=\Psi x_L \tag{8}$$

When considering the magnet rotation, the position of magnet 1 with regard to magnet 2 shown in Eq. (9) is determined in the coordinate system (x,y) as in Fig. 1(b), which takes the unstable equilibrium position as the origin.

$$\boldsymbol{r_{12}}=r_{12,i}\boldsymbol{i}+r_{12,j}\boldsymbol{j}=[x_L+asin(\theta)\,]\boldsymbol{i}+[-H-a(1-cos(\theta)\,)]\boldsymbol{j} \tag{9}$$

Here, the characters in bold indicate vectors, $\boldsymbol{i}$ and $\boldsymbol{j}$ are unit vectors of the Cartesian coordinate system (x,y), a is the half length of the magnet, and H is the center to center distance between the two magnets.

The magnetic force on magnet 1 induced by magnet 2 is then given in Eq. (10).

$$\boldsymbol{F_{21}}=\frac{3\mu_0}{4\pi|\boldsymbol{r_{21}}|^4}\{(\bar{\boldsymbol{r}}_{\boldsymbol{21}}\times\boldsymbol{\mu_2})\times\boldsymbol{\mu_1}+(\bar{\boldsymbol{r}}_{\boldsymbol{21}}\times\boldsymbol{\mu_1})\times\boldsymbol{\mu_2}-2\bar{\boldsymbol{r}}_{\boldsymbol{21}}(\boldsymbol{\mu_2}\cdot\boldsymbol{\mu_1})+5\bar{\boldsymbol{r}}_{\boldsymbol{21}}[(\bar{\boldsymbol{r}}_{\boldsymbol{21}}\times\boldsymbol{\mu_2})\cdot(\bar{\boldsymbol{r}}_{\boldsymbol{21}}\times\boldsymbol{\mu_1})]\} \tag{10}$$

The overbar indicates normalization of the vectors, μ_0 is the free permeability constant, which is $\mu_0=4\pi\times10^{-7}N/A^2$, $\boldsymbol{\mu_1}$ and $\boldsymbol{\mu_2}$ are respectively the moment of magnet 1 and 2, which are calculated by Eq. (11a,b).

$$\boldsymbol{\mu_1}=-M_1V_1sin\theta\,\boldsymbol{i}+M_1V_1cos\theta\boldsymbol{j};\quad\boldsymbol{\mu_2}=-M_2V_2\boldsymbol{j} \tag{11a,b}$$

In Eq. (11), M_1 and M_2 are magnetization of magnets 1 and 2; V_1 and V_2 correspond to the volume of magnets 1 and 2.

For the clamped beam shown in Fig. 1(a), the magnetic force acting on the magnet 1 along the transverse x direction is computed to be [10]

$$F_{21}=\frac{3\mu_0M_1V_1M_2V_2}{4\pi}\frac{-5r_{12,i}\left(r_{12,i}cos\theta+r_{12,j}sin\theta\right)r_{12,i}+\left(4r_{12,i}cos\theta+r_{12,j}sin\theta\right)\left(r_{12,i}^2+r_{12,j}^2\right)}{\left(r_{12,i}^2+r_{12,j}^2\right)^{7/2}} \tag{12}$$

Substituting the expression of magnet force Eq. (12) to the governing equation in Eq. (1) with the initial conditions Eq. (2) and periodic impulsive excitation Eq. (3), the nonlinear system dynamics of the energy harvesting system are able to be examined.

2.2. Discussions on dynamics of nonlinear energy harvesters under periodic impulse excitation

Given the model established in Section 2.1, two systems are selected to investigate the dynamic characteristics of the nonlinear energy harvester subjected to periodic impulse excitation. The parameters used in system 1 are shown in Table 1. The system parameters selected for system 1 induce bistability and thus result in considerably distinguished dynamics between low and large amplitude vibrations. The magnet distance for system 1 is decreased by 5% to construct system 2. Thus, system 2 possesses stable equilibria that are further spaced apart due to the greater repulsive force. The frequency of the periodic impulse in Fig. 1(b) is hereafter referred to as the periodic impulse frequency. In the following investigations, the periodic impulse frequency is changed over the range of 6 Hz to 15 Hz. The impulse magnitudes are selected to be 0.06 m/s and 0.075 m/s for systems 1 and 2, respectively, which are sufficient to trigger snap-through vibration over at least a portion of the frequency spectrum. Two impulse directions are taken into

Table 1
Identified system parameters for the nonlinear system.

m(g)	c(N s/m)	k_1(N/m)	k_3(MN/m^3)	ρ(kg/m^3)	A(mm^2)	l(mm)	a(mm)
10.6	0.01	213	2	3500	7.5	34	3.175
C_p(nF)	α(mN/V)	H(mm)	C_r(μF)	M(MA/m)	V(cm^3)	R(kΩ)	
44	0.07	21	47	1.25	0.768	560	

account. Specifically, the impulse direction with negative impulse velocity is defined as the negative direction. Correspondingly, the opposite direction is specified as a positive impulse direction. The fourth-order Runge-Kutta numerical method is utilized to determine the responses from Eq. (1). The initial conditions are given in Eq. (2). The simulation duration is chosen to be 500 impulsive periods to ensure the steady-state responses are identified.

Fig. 2 investigates the characteristics of the dynamic responses when the nonlinear energy harvesting system is subjected to periodic impulse excitation. As shown in Fig. 2(a), similar to the frequency responses under harmonic excitation [3,4], for lower periodic impulse frequencies the small amplitude intrawell vibration is induced for both systems. With the increase of the periodic impulse frequency to around 9 Hz, there is a discrete increase in the displacement amplitude by almost 10 times, illustrating the generation of snap-through vibration. For the periodic impulse frequency greater than 12 Hz, the intrawell vibration is induced for both systems. The decrease in magnet distance in system 2 compared to system 1 leads to a higher nonlinearity, which corresponds to a larger static equilibrium value. Since the snap-through vibration jumps between two static equilibrium positions, the displacement amplitude generated for system 2 is more than those amplitudes induced for system 1 at the same periodic impulse frequencies.

Moreover, according to the Fourier transform of system 1 displacement in Fig. 2(b), the response at each periodic impulse frequency is dominated by a single frequency, which is an integer multiple of the periodic impulse frequency. In the following discussions, the ratio of the dominant frequency of the response and the periodic impulse frequency is termed the dominant frequency ratio. As seen in Fig. 2(b), the dominant frequency ratio shifts from two to one when the periodic impulse frequency is changed from 6 Hz to 10 Hz. The transition occurs around 8 Hz. As shown in the frequency responses for system 1 in Fig. 2(c), the dominant frequency ratio is two at a periodic impulse frequency of 7 Hz and changes to a ratio of one at 8 Hz. In addition, around the periodic impulse frequency that the transition happens, the displacement amplitude at the dominant frequency ratio is slightly greater than the second-largest displacement amplitude, which implies a combined frequency influence in the responses.

One noticeable contrast between responses generated from positive and negative impulses for two systems lies in the high-energy snap-through vibration. As shown in Fig. 2(a), in terms of snap-through vibration, the negative impulse can more often generate the snap-through vibration at lower frequencies for both systems. Fig. 3(a) and (b) respectively show the time series of displacement and velocity for system 1 at the periodic impulse frequency 9 Hz with two impulse directions. At time $t = 0^+$, the application of the negative impulse introduces a negative velocity in the system. According to the initial conditions shown in Eq. (2) and the changes of states in Eq. (3), the negative impulse here is defined as $I_n = -42$ mm/s. The negative sign '-' indicates the impulse is applied towards the negative x axis as in Fig. 1(c). Comparatively, the positive impulse is $I_p = 42$ mm/s exerts an impulse in the positive x axis.

Fig. 3(c) displays the potential energy of the nonlinear system and total energy of the time series derived from Fig. 3(a). It can be seen from Fig. 3(c) that the potential energy around the positive static equilibrium is asymmetric. As such, the magnitudes of the beam tip velocity generated by the two impulse directions are distinct at every moment except for times $t = 0$ and $t = T_n$ in Fig. 3(a) and (b). Here T_n corresponds to the period of the beam's free vibration. As shown in Fig. 3(b), at the instant before the application of the impulse at $t = T$, the values of the velocities associated with the two impulse directions are negative, which indicates that the beam velocity is in the negative direction of the x axis. Based on the change of velocity caused by the impulse shown in Eq. (3), the application of the negative impulse increases the magnitude of the beam velocity by 42 mm/s. Yet, the velocity magnitude associated with the positive impulse direction decreases, as in Fig. 3(b). Thus, two opposite effects may be induced by the two impulse directions.

The total energy changes for the vibration shown in Fig. 3(a) are presented in Fig. 3(c) as functions of the displacement to permit contrast with the potential energy profile. For the response induced by the negative impulse direction, the application of the impulse keeps injecting kinetic energy into the system. The accumulated energy helps the beam escape the potential energy barrier and start generating snap-through vibration after 3 cycles of excitation. In contrast, the kinetic energy for the system excited by the positive impulse decreases in time, seen by the confinement of the displacement to positions within one well of the potential energy profile. In addition, because the magnitudes of the displacement and velocity at $t = T_n$ are the same for the two impulse directions. When the periodic impulse frequency is close to the natural frequency of the vibration system $1/T_n$, the velocities generated by the two impulse directions are around same magnitude and in opposite direction. As such, both impulse directions may generate snap-through vibration, such as frequencies around 10 Hz for system 1 and frequencies around 11 Hz for system 2 in Fig. 2(a).

According to these preliminary observations, both high amplitude snap-through and low amplitude intrawell vibrations may be

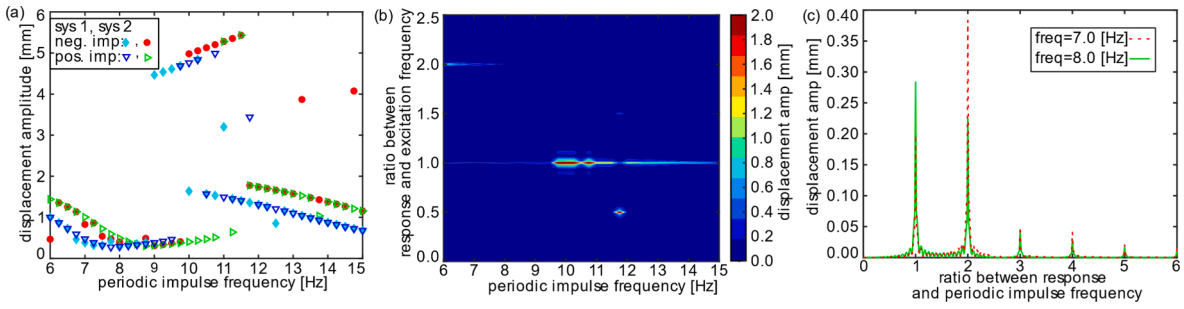

Fig. 2. (a) Frequency responses of beam tip displacement amplitude for systems 1 and 2 under negative and positive directions of the periodic impulse. (b) Fourier transform of displacement amplitude for system 1. (c) Fourier transform of displacement amplitude for system 1 at frequencies 7.5 Hz and 8 Hz.

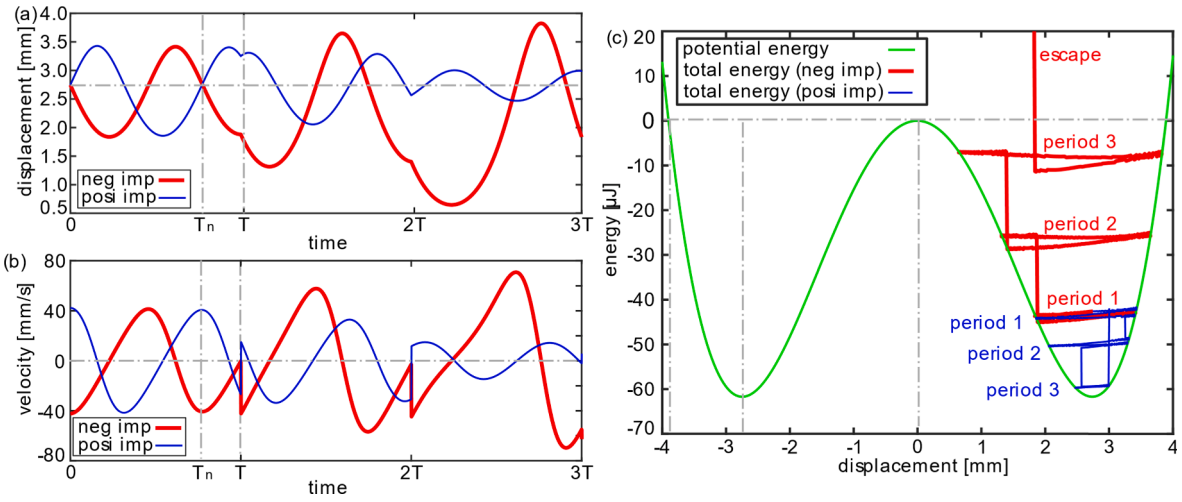

Fig. 3. (a) Displacement and (b) velocity time series for system 1. (c) Potential energy plot and total energy changes in first three periods for system 1. The excitation condition is a periodic impulse at 9 Hz with impulse magnitude 42 mm/s in both positive and negative impulse directions.

generated with a dominant frequency component by the periodic impulse excitation. The distinct dynamic regimes have significant implications on energy harvesting effectiveness. In the following sections, these findings are utilized to construct a reduced order surrogate model to improve one's ability to design and analyze the dynamics of the nonlinear energy harvesting systems.

3. Experimental validation

3.1. Experimental system description and identification

To experimentally validate the key findings described above, the platform shown in the schematic of Fig. 1(a) is realized in the laboratory as seen in Fig. 4. Fig. 4(a) presents the piezomagnetoelastic system studied here. The piezoelectric beam is a bimorph made by sequential layers of FR4, PZT-5H, and steel shim. The PZT-5H layer covers part of the beam for sake of robustness and minimizing the brittle PZT usage. The beam is clamped to an aluminum base, which is affixed to the mounting table. A permanent magnet is secured in a magnet holder and is attached to the free end of the beam. The total tip mass M_0 is the combination of the magnet and magnet holder. The other magnet is mounted adjacent to the beam free end, and is oriented so as to introduce repulsive magnet force upon the beam tip. Two displacement laser sensors (Micro-Epsilon ILD-1420) are utilized to measure the absolute displacements of the shaker table and the beam tip. A standard rectifier bridge (1 N4148 diodes) is connected to the piezoelectric beam to convert an AC signal to a DC signal. Following the bridge, a smoothing capacitor C_r and resistive load R are utilized to quantify the harvested electric energy.

Fig. 4(b) shows the equipment to generate the periodic impulse excitation. In Fig. 4(b), the mounting table is fixed on a base that can provide necessary stiffness and damping. The mounting table is struck by an L-shape aluminum frame. The L-shape aluminum

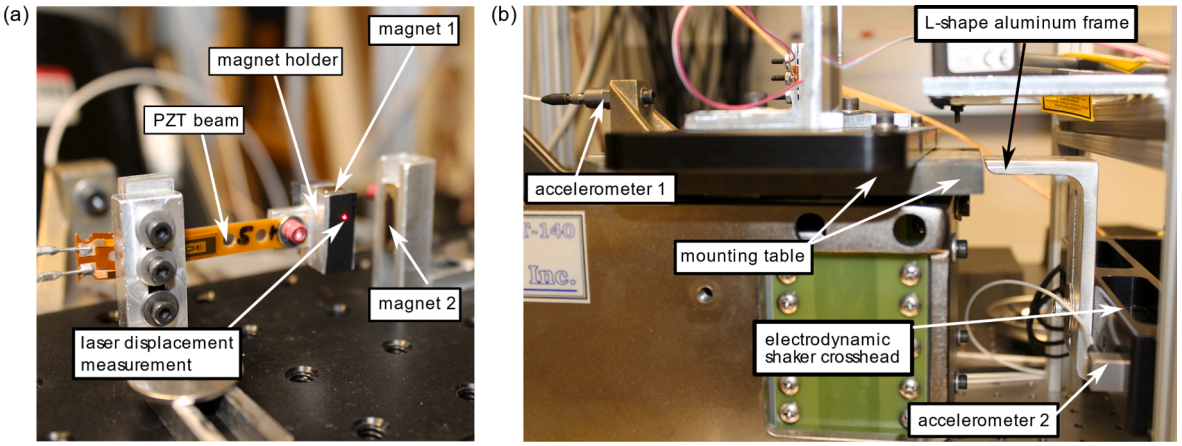

Fig. 4. Photos of experimental setup. (a) Nonlinear energy harvester. (b) Equipment to generate periodic impulse excitation.

frame is installed at the crosshead of an electrodynamic shaker table (APS Dynamics 400). The gap between the L-shape aluminum frame and the mounting table is maintained at 2 mm before the beginning of each experiment. The electrodynamic shaker table is driven by a controlled harmonic signal provided by a controller (Vibration Research Controller VR9500) and amplifier (Crown XLS 2500). An accelerometer (PCB Piezotronics 333B40) is utilized to collect the feedback signal for the controller. The periodic impulse base acceleration on the mounting table is generated by the impact from the aluminum frame striking the mounting table. The opposite impulse direction is achieved by rotating the mounting table by 180°. The accelerometer (PCB Piezotronics 352C04) is installed to measure the frequency and magnitude of the impulse acceleration.

For the piezomagnetoelastic system, the equivalent lumped mass m and linear stiffness k_1 are determined according to the classical relations [11]. The logarithmic decrement method is then applied to determine the viscous damping. With the measured static equilibrium position x^* and magnet distance H, the magnetic force at the equilibrium position F_{21}^* can be determined by Eqs. (8), (9), and (12). Therefore, according to Eq. (1a), the nonlinear term k_3 is calculated by Eq. (13).

$$k_1 x^* + k_3 (x^*)^3 = F_{21}^* \tag{13}$$

The parameters of the nonlinear energy harvester platform examined in the laboratory are provided in Table 1.

3.2. Model validation and discussions

In order to validate the efficacy of the model established in Section 2, the experimental setup shown in Fig. 4 is utilized. The influences of impulse direction on the generation of snap-through vibrations and frequency dominant responses are closely considered in experiments. Five frequencies are selected to excite the system with six impulse magnitudes in two impulse directions.

Table 2 shows the experimental and numerical results that indicate the vibration type and the dominant frequency component. In experiments, the recorded beam tip displacement time series from the laser sensors is utilized to ensure the beam displaces away from the static equilibrium position x^* for each excitation condition. The impulse magnitude characterized by the velocity change is integrated from the impulse acceleration acquired from experiments. The integrated velocities in the dimension of m/s are rounded to 3 significant digits after the decimal to ensure simulation accuracy. The signs '+' and '-' indicate the impulse direction, while vibration

Table 2
Comparison between experiments and simulations. Impulse demonstrates impulse magnitude and impulse direction. The positive sign '+' indicates positive impulse direction and '-' indicates negative impulse direction. Vibration type 1 represents intrawell vibration, 0 represents snap-through vibration. Frequency ratio is the dominant frequency ratio, determined from the ratio between response dominant frequency and periodic impulse frequency. Light grey shading indicates differences in generating snap-through vibration by two impulse directions. Dark grey shading indicates discrepancies between simulations and experiments in predicting vibration type and frequency ratio.

f_{exc} [Hz]	Classification	Experiment												Simulation											
6	Impulse I	67		79		90		100		113		133		67		79		90		100		113		133	
	[mm/s]	+	-	+	-	+	-	+	-	+	-	+	-	+	-	+	-	+	-	+	-	+	-	+	-
	Vib. type	1	1	1	1	1	1	1	0	0	0	0	0	1	1	1	1	1	1	0	0	0	0	0	0
	Freq. ratio	2	2	2	2	2	2	2	1.5	1.5	1.5	1.5	1.5	2	2	2	2	2	2	2	2	2	2	2	2
7	Impulse I	67		88		107		114		118		130		67		88		107		114		118		130	
	[mm/s]	+	-	+	-	+	-	+	-	+	-	+	-	+	-	+	-	+	-	+	-	+	-	+	-
	Vib. type	1	1	1	1	1	1	1	1	1	0	1	0	1	1	1	1	1	1	1	1	0	0	0	0
	Freq. ratio	2	2	2	2	2	2	2	2	2	1	2	1	2	2	2	2	2	2	2	2	0	0	2	2
8	Impulse I	54		60		65		68		76		85		54		60		65		68		76		85	
	[mm/s]	+	-	+	-	+	-	+	-	+	-	+	-	+	-	+	-	+	-	+	-	+	-	+	-
	Vib. type	1	1	1	1	1	1	1	0	1	0	1	0	1	1	1	1	1	1	1	1	1	1	1	1
	Freq. ratio	2	2	2	2	2	2	2	1	2	1	2	1	1	1	1	1	1	1	1	1	1	1	1.5	1
9	Impulse I	30		46		52		59		64		67		30		46		52		59		64		67	
	[mm/s]	+	-	+	-	+	-	+	-	+	-	+	-	+	-	+	-	+	-	+	-	+	-	+	-
	Vib. type	1	1	1	1	1	1	1	0	0	0	0	0	1	1	1	1	1	1	1	1	1	0	1	0
	Freq. ratio	2	2	1	2	1	2	1	1	1	1	1	1	1	1	1	1	1	1	1	1	1	1	1	1
10	Impulse I	27		36		54		66		85				27		36		54		66		85			
	[mm/s]	+	-	+	-	+	-	+	-	+	-			+	-	+	-	+	-	+	-	+	-		
	Vib. type	1	1	1	1	1	1	1	1	1	1			1	1	1	1	1	1	1	0	0	0		
	Freq. ratio	1	1	1	1	1	1	1	1	1	1			1	1	1	1	1	1	1	1	1	1		

type 1 is intrawell and type 0 is snap-through vibration. In experiments, intrawell vibrations result for periodic impulse frequencies from 6 Hz to 10 Hz at lower impulse magnitudes, such as 52 mm/s at 9 Hz. With the increase of the impulse magnitude to 59 mm/s, snap-through vibrations are then generated at 9 Hz for the impulse in the negative x direction. Further increasing the impulse magnitude to 100 mm/s in the negative x direction, snap-through vibrations can be realized at 6 Hz. Comparing the snap-through vibrations generated by the two impulse directions, the same impulse magnitude with the negative direction is seen to more often lead to snap-through vibrations, which is highlighted by the light grey background in Table 2. For example, for periodic impulse frequency of 8 Hz and impulse magnitude greater than 68 mm/s, the impulses with negative direction always lead to snap-through vibrations. In comparison, positive impulses generate intrawell vibrations. At 9 Hz, both impulse directions generate snap-through vibrations when the impulse magnitude is greater than 64 mm/s, which indicates a decreased influence of impulse directions on snap-through vibration at higher periodic impulse frequency as discussed in Section 2.2.

Further comparing the simulations with experiments in Table 2, the numerical model is less accurate in reproducing experimental behaviors for large magnitudes of the impulse. The model predictions that disagree with the experiments are highlighted with dark shaded background in Table 2. As shown in the comparison of simulated and measured displacement time series in Fig. 5(a), the system realizes the intrawell vibration with periodic impulses at 10 Hz and 54 mm/s magnitude, and good agreement is seen between experiment and simulation. Yet, when the impulse magnitude is great enough to generate snap-through vibration, such as 67 mm/s at 9 Hz in Fig. 5(b), the beam slightly crosses the unstable equilibrium in the experiment whereas numerical responses illustrate a more symmetric snap-through vibration between two stable equilibria. The use of reinforcing FR4 layers in the piezoelectric beam may cause the discrepancies for large displacement amplitude response since FR4 is a viscoelastic fiber-reinforced polymer with nonlinear damping and stiffness that is challenging to characterize in full [35,32]. The present model assumes linear damping and linear elasticity, which may not completely capture such dynamic behaviors in regimes of large strains and strain rates associated with the largest amplitude of snap-through. Another factor that may cause the discrepancies between experiment and simulation is the non-ideal duration of the impulse. In experiments, the impulse occurs over around 8 ms (around 8% of the excitation period) which is a small but finite proportion of the excitation conditions. Yet, despite these distinguishing points between the model results and experimental findings, agreement is obtained for the great majority of cases studied in Table 2, validating the composition of the theoretical model for the many cases of interest considered here.

In terms of the dominant frequency component in response, the dominant frequency ratio shifts from two to one near the periodic impulse frequency 9 Hz in experiments in contrast to 8 Hz in simulations. As shown in Fig. 5(c), the dominant frequency ratio is two when the periodic impulse frequency and impulse magnitude are 8 Hz and 85 mm/s in the positive direction respectively. A transition occurs to a dominant frequency ratio of one at periodic impulse frequency 9 Hz and impulse magnitude 59 mm/s in the positive direction. Similar to Fig. 2(c), the displacement amplitude at the dominant frequency component is slightly greater than the second-largest displacement amplitude at periodic impulse frequency 9 Hz. Since the numerical model adopts assumptions such as lumped parameters and viscous damping to characterize the system, the small variation in displacement amplitude at dominant frequency ratios one and two may not be completely captured. Given the definition on the response dominant frequency, the discrepancy in capturing the displacement amplitude may result in the variations in predicting the dominant frequency ratio at periodic impulse frequencies 8 and 9 Hz in simulations.

The optimal resistance for DC power collection estimated by the model is then confirmed. Table 3 shows the optimal resistances from experiments and simulations. In experiments, five cases are selected to assess agreement across all vibration types and ratios of the dominant response frequency. Compared with the experiments, the simulations provide good approximations on optimal resistances for frequencies from 6 Hz to 10 Hz, although error increases near periodic impulse excitations around 8 Hz where transitions occur in the values of the dominant frequency ratio (see also Table 2). Since the response frequency influences optimal resistance

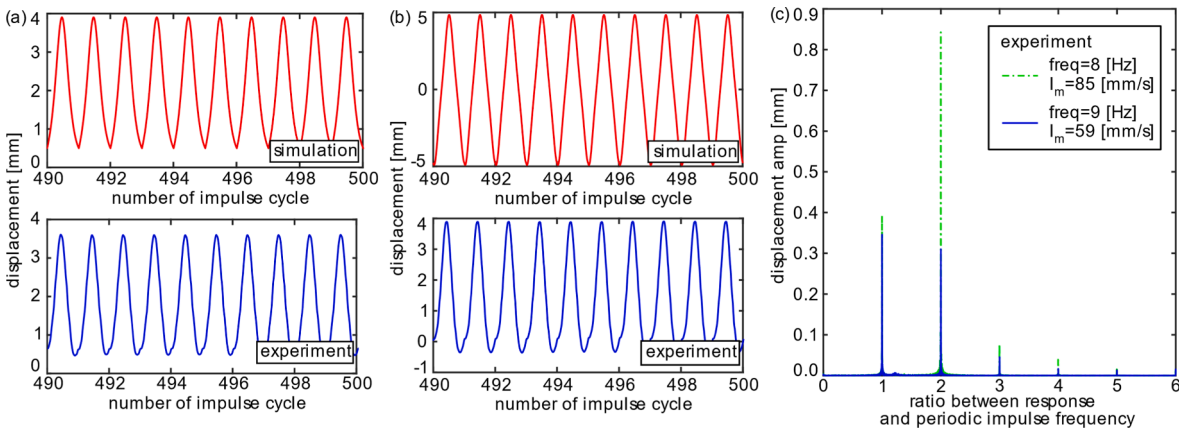

Fig. 5. Numerical and experimental displacement time series at (a) periodic impulse frequency 10 Hz and impulse magnitude 0.054 m/s in the positive x direction, and (b) periodic impulse frequency 9 Hz and impulse magnitude 0.067 m/s in the negative x direction. (c) Fourier transform of experimentally measured displacement amplitude at frequencies 8 Hz and 9 Hz respectively with impulse magnitude 85 mm/s and 59 mm/s in the positive x direction.

Table 3
Comparison between experiment and simulation for optimal resistance.

Periodic impulse frequency [Hz]	Impulse I [mm/s]	Optimal resistance [kΩ]	
		Experiment	Simulation
6	79	470	475
7	67	560	409
8	54	470	356
9	67	509	625
10	54	560	596

selections [3,4], for excitation frequencies around 8 Hz the differences of optimal resistance between simulations and experiments are within 25%.

Overall, the experimental setup provides means to validate and classify the simulations of nonlinear energy harvesting system dynamics when subjected to periodic impulses. This foundation is essential for subsequent coupling of the modeling approach with a machine learning prediction framework that helps create insight on the relative merits on the dynamic regimes for vibration energy harvesting.

4. Physics-guided machine learning model for optimal design strategies

From the perspectives of system design, individual simulations are an inefficient way to identify the optimality by gradient descent methods. Furthermore, the non-smooth and discretized nature of the dynamic behaviors encourage a classification approach that distinguishes parametric combinations for the contributions to best performing system configurations. In this section, a machine learning algorithm is integrated with the theoretical model to assist in identifying mechanisms and design practices that lead to maximum DC charging power in impulse-excited nonlinear vibration energy harvesting systems.

4.1. Physics-guided machine learning model for dynamics characterization

4.1.1. Establishment of a physics-guided machine learning model

For high-dimensional and multiphysics problems in science and engineering, reduced-order models (ROMs) are employed to minimize computational needs for only those dynamic behaviors that culminate in the great proportion of meaningful system responses. The ROMs are established by principal components analysis or dynamic mode decomposition to project the intricate governing equations or responses to a low-dimensional and often-linear subspace. Yet, the prediction accuracy may be limited as a consequence of simplification. With the emergent capabilities in data science, machine learning algorithms integrated with theoretical models aim to construct ROMs that are more computationally efficient as well as better low-dimensional representations of an intricate system dynamics [37]. One approach to constructing the physics-guided ROMs is to build a surrogate model for a full-order model

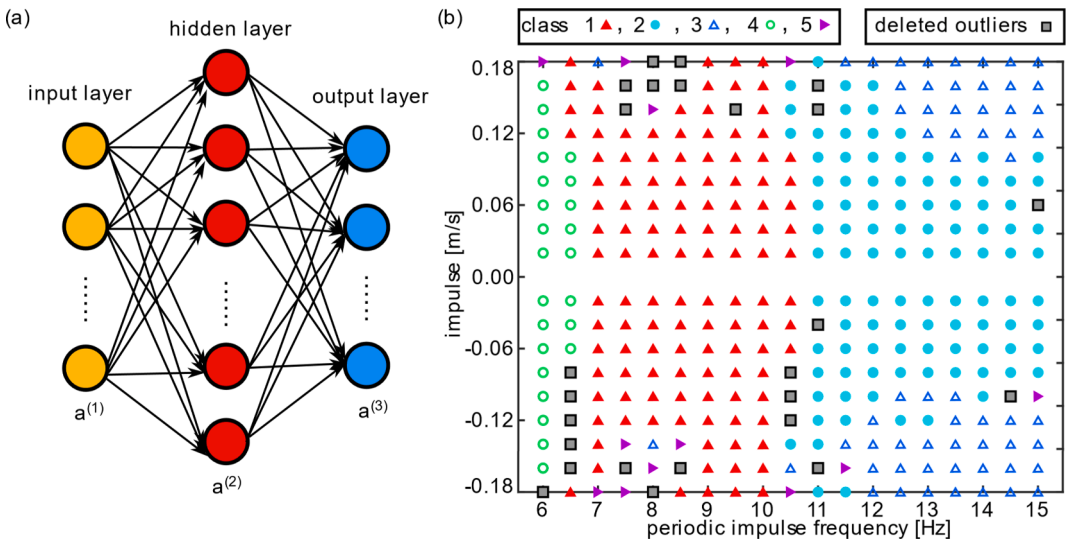

Fig. 6. (a) Neural network with 3 layers. (b) Classification results for damping constant 0.01 N.s/m and magnet gap 20.55 mm from simulation as functions of the periodic impulse frequency and impulse magnitude in two directions. Classes 1, 2, and 4 respectively represent intrawell vibration with dominant frequency ratio two, one, and three, class 3 represents snap-through vibration with dominant frequency ratio one, and class 5 represents chaotic vibration. The outliers belong to other classes with small occurrence possibility.

[37]. For example, Chen et al. [6] exploited the Support Vector Machine algorithm to construct a surrogate reduced-order model to predict the limit cycle oscillation of nonlinear aeroelastic systems. In the following discussions, supervised learning is selected to help build a surrogate model that maps the input design parameters to output dynamics characterized by the vibration type and the dominant frequency ratio.

There are several classification algorithms in supervised learning , such as logistic regression, decision trees, support vector machines, and neural networks. Compared with other methods, neural networks infer the nonlinear and complex relationships among states and parameters with less manual intervention to craft suitable basis functions [24,1]. Therefore, the neural network algorithm is selected to help build the mapping functions for the surrogate model of the impulse-excited nonlinear vibration energy harvesting system. The network architecture utilized in the study is a three-layer neural network as shown in Fig. 6(a), which includes an input layer, one hidden layer, and output layer. The units on the input layer are defined by the features of the training examples. Features are design parameters and other factors that are initially assumed to be correlated with outputs. The hidden units create the nonlinear mapping between the input and output layers. The number of units in the hidden layer is chosen to ensure a high accuracy of the prediction results. The output units identify the classes of a problem.

In this research, the inputs corresponds to design parameters of the nonlinear energy harvesting systems, while the outputs are the classes characterized by the vibration type and the dominant frequency ratio. In this way, we seek to correlate the system dynamic behaviors associated with intrawell and snap-through vibration with the periodicity of the responses resulting from the excitation and design parameter combinations. Specifically, four design parameters are selected, which are impulse magnitude I, periodic impulse frequency f_{exc}, magnet gap H, and damping constant c. The input features for the neural network is shown in Eq. (14). For the given problem, a hidden layer with 25 units is tested to provide satisfying prediction results.

$$\boldsymbol{x} = \begin{bmatrix} \overline{f}_{exc} & \overline{I} & \overline{H} & \overline{c} \end{bmatrix} \tag{14}$$

In Eq. (14), the overbar indicates the normalization of features to ensure each feature is on a similar scale. Here the normalization is carried out by subtracting the minimum value and dividing by the maximum value for each respective feature to scale the values from zero to one.

The established model in Section 2.1 is utilized to generate the instances for training and cross validating the neural network. In simulations, the impulse I varies from -0.18 m/s to 0.18 m/s to consider the impulse applied in two directions defined in Section 2, the periodic impulse frequency f_{exc} ranges from 6 Hz to 15 Hz, the magnet gap H is selected from 19.55 mm to 21.55 mm, and the damping c increases from 0.005 N·s/m to 0.05 N·s/m. The increments assigned for the four parameters are 0.02 m/s, 0.5 Hz, 0.01 mm, and 0.005 N·s/m respectively. In total, 75,810 simulation examples are generated.

Before training the neural network, the numbers of the occurrence for each class are counted. After ordering the occurrence number from high to low, the accumulated summation is calculated. Once the summation of the examples is higher than 95% of the total examples, the classes with occurrence less than 5% are deleted. After the removal of classes with such insignificant probability of occurrence, by changing the 4 input parameters, there remain 68,321 simulation examples that are classified into 6 distinct classes. Here class 1 refers to intrawell responses with dominant frequency ratio two; class 2 refers to intrawell responses with dominant frequency ratio one; class 3 refers to snap-through vibration with dominant frequency ratio one; class 4 refers to intrawell vibration with dominant frequency ratio three; class 5 refers to chaotic vibration; and class 6 refers to intrawell vibration with a dominant frequency ratio of four. Fig. 6(b) shows the numerical classification results by changing the periodic impulse frequency from 6 Hz to 15 Hz and impulse magnitude from 0 to 0.18 m/s in two directions with the values of magnet gap as 20.55 mm and damping as 0.01 N.s/m. With these values of magnet gap and viscous damping, there are no examples of class 6 in this example dataset. The classes shown in rectangles in Fig. 6(b) belong to 6 additional classes that have insignificant probabilities to occur, such as intrawell vibration with dominant frequency ratio of one-half. According to Fig. 6(b), the remaining examples exemplify the predominant dynamic characteristics of the system.

With the remaining simulation examples, 70% of the examples are selected to construct the training set, the remaining 30% are taken as the cross-validation set. For the training set, as shown in Fig. 6(b), the number of training examples in each class may have a large influence on the predictor model. This is termed as an imbalanced classification problem in machine learning. For instance, for the given problem, the number of training examples in class 6 is 998, which is 6.4 % of the number of training examples in class 1. To avoid imbalanced datasets, the method of oversampling is adopted, which duplicates random instances of the minority class to balance the number of data in each class. For the given problem, when the number of examples in a class is less than 5% of the total number of examples in the training set, the class is defined as the minority class and the examples in the minor class are randomly selected to duplicate the new examples for the class.

Mathematically, training a neural network is to determine the weights $\boldsymbol{\Theta}$ associated with the minimum value of the cost function. For classification problems, the cost function defined in Eq. (15) is utilized to assess the difference of the k-th output unit for the input features of the i-th training example. Once trained, providing new examples $\boldsymbol{x}^i$ to the functions in Eq. (16) leads to prediction of the output classifier $\boldsymbol{a}^{(3)}$, whereby the established model is referred to as a "predictor model".

$$\mathrm{Cost}\left(\left(h_{\boldsymbol{\Theta}}(\boldsymbol{x}^i)\right)_k, y_k^i\right) = \begin{cases} -log\left(h_{\boldsymbol{\Theta}}(\boldsymbol{x}^i)\right)_k, & \text{if } y_k^i = 1 \\ -log\left(1 - h_{\boldsymbol{\Theta}}(\boldsymbol{x}^i)\right)_k, & \text{if } y_k^i = 0 \end{cases} \tag{15}$$

$$\boldsymbol{a}^{(1)} = \boldsymbol{x}^i;\ \boldsymbol{b}^{(1)} = \begin{bmatrix} 1 & \boldsymbol{a}^{(1)} \end{bmatrix};\ \boldsymbol{z}^{(2)} = \boldsymbol{\Theta}^{(1)}\boldsymbol{b}^{(1)};\ \boldsymbol{a}^{(2)} = g\left(\boldsymbol{z}^{(2)}\right);\ \boldsymbol{b}^{(2)} = \begin{bmatrix} 1 & \boldsymbol{a}^{(2)} \end{bmatrix};$$
$$\boldsymbol{z}^{(3)} = \boldsymbol{\Theta}^{(2)}\boldsymbol{b}^{(2)};\ \boldsymbol{a}^{(3)} = g\left(\boldsymbol{z}^{(3)}\right);\ h_{\boldsymbol{\Theta}}\left(\boldsymbol{x}^i\right) = \boldsymbol{a}^{(3)};\ g(z) = \frac{1}{1+e^{-z}}; \tag{16a,b,c,d,e,f,g,h,i}$$

where $\boldsymbol{x}^i$ indicates the input features of the i-th training example; $h_{\boldsymbol{\Theta}}(\boldsymbol{x}^i)$ estimates the probability that $\boldsymbol{x}^i$ belongs to each class and is determined by the forward propagation as in Eq. (16 a-d); a constant 1 is added in the forward propagation to account for the bias existing in the system; $(h_{\boldsymbol{\Theta}}(\boldsymbol{x}^i))_k$ is the predicted probability that the input $\boldsymbol{x}^i$ is associated with class k; y_k^i is the labeled value to demonstrate the class that the input $\boldsymbol{x}^i$ is truly in, which is 1 if the input features $\boldsymbol{x}^i$ is in class k, otherwise $y_k^i = 0$; $\boldsymbol{\Theta}^{(1)}$ and $\boldsymbol{\Theta}^{(2)}$ are weights to be determined through the training process, which are randomly initialized at the start as matrices with the size of $h \times n$ and $m \times (h+1)$; function g is employed to satisfy the (0, 1) limits of the classifier y_k^i. In the study, the sigmoid function in Eq. (16e) is utilized to map inputs to outputs in the range 0 to 1.

With the predicted probability $h_{\boldsymbol{\Theta}}(\boldsymbol{x}^i)$, the class with the maximum probability is the predicted class for the i-th training example by the neural network. For the training example $\boldsymbol{x}^i$ labeled as in class k, thus $y_k^i = 1$. If $(h_{\boldsymbol{\Theta}}(\boldsymbol{x}^i))_k$ predicts a high possibility around 1 for class k, the cost function in Eq. (15) is corresponding to a small value around zero. Otherwise, a large value is assigned as a penalty to the cost function. As such, the differences between the labeled and predicted value are measured.

The cost function in Eq. (15) can be consolidated to a more compact form as in Eq. (17).

$$J_{ik}(\Theta) = -\left[y_k^i log\left(h_{\boldsymbol{\Theta}}(\boldsymbol{x}^i)\right)_k + \left(1-y_k^i\right) log\left(1-h_{\boldsymbol{\Theta}}(\boldsymbol{x}^i)\right)_k\right] \tag{17}$$

Further, the total cost function for all training examples and all output units for training the neural network is defined in Eq. (18),

$$J(\Theta) = -\frac{1}{N_t}\left[\sum_{i=1}^{N_t}\sum_{k=1}^{K} J_{ik}(\Theta)\right] \tag{18}$$

where N_t is the total number of training examples; K is the total number of output units, which is associated with the total number of classes included in the problem.

An unconstrained minimization function is used to find the minimum of Eq. (18) by tailoring the weight matrices. The inputs for the minimization function are the cost function defined in Eq. (18) and the random initialization of matrices $\boldsymbol{\Theta}^{(1)}$ and $\boldsymbol{\Theta}^{(2)}$. The corresponding outputs are the trained matrices $\boldsymbol{\Theta}^{(1)}$ and $\boldsymbol{\Theta}^{(2)}$ that are associated with minimum cost function value. With the trained matrices $\boldsymbol{\Theta}^{(1)}$ and $\boldsymbol{\Theta}^{(2)}$, the forward propagation shown in Eq. (16 a-d) can be employed to predict the class for new input features.

4.1.2. *Assessment of the effectiveness of the physics-guided machine learning model*

In order to assess the effectiveness of the mapping formulated by the neural network, the accuracy and F_1 score are introduced to quantitively measure the predictor model effectiveness. Eq. (19) shows the confusion matrix for the multi-class classification problem. Element M_{ij} indicates the number of examples in class i that are incorrectly identified as class j when $i \neq j$. The diagonal elements demonstrate the number of accurate predictions. With the information provided from the confusion matrix, the accuracy, precision,

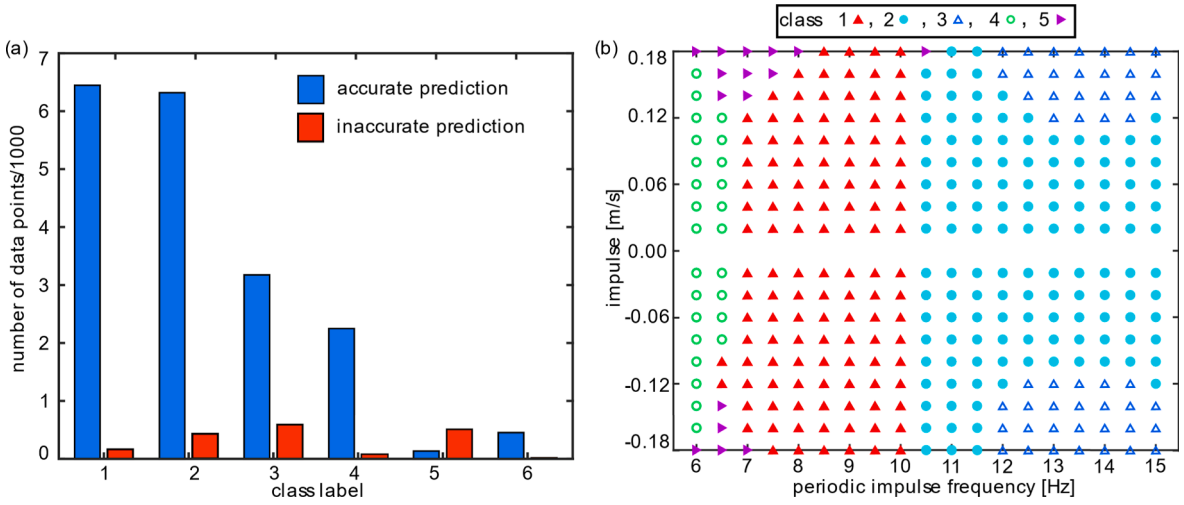

Fig. 7. (a) Assessment of class prediction accuracy by the supervised predictor model. (b) Classification results for damping constant 0.01 N.s/m and magnet gap 20.55 mm as functions of periodic impulse frequency and magnitude applied in two directions. Classes 1, 2, and 4 respectively represent intrawell vibration with dominant frequency ratio two, one, and three, class 3 represents snap-through vibration with dominant frequency ratio one, and class 5 represents chaotic vibration.

and recall are defined in Eq. (20 a-c). The accuracy is a measure of correctly identified cases, which is the ratio of the correctly predicted cases to the total number of validation cases. Precision and recall are the ratios between the number of correctly identified instances in a class against the total number of predicted instances and against the total number of the actual cases in the class. For a multi-classification problem, the averages among all classes defined in Eq. (20b,c) are taken as the overall precision and recall for the problem. The F1 score identified in Eq. (20d) is the weighted average of the precision and recall to better measure the incorrectly classified cases for imbalanced classification problems.

$$confusion\ matrix = \begin{bmatrix} M_{11} & M_{12} & M_{13} & M_{14} & M_{15} & M_{16} \\ M_{21} & M_{22} & M_{23} & M_{24} & M_{25} & M_{26} \\ M_{31} & M_{32} & M_{33} & M_{34} & M_{35} & M_{36} \\ M_{41} & M_{42} & M_{43} & M_{44} & M_{45} & M_{46} \\ M_{51} & M_{52} & M_{53} & M_{54} & M_{55} & M_{56} \\ M_{61} & M_{62} & M_{63} & M_{64} & M_{65} & M_{66} \end{bmatrix} \tag{19}$$

$$accuracy = \frac{\sum_{m=1}^{6} M_{mm}}{\sum_{i=1}^{6}\sum_{j=1}^{6} M_{ij}};\quad precision = \frac{1}{6}\sum_{m=1}^{6}\frac{M_{mm}}{\sum_{i=1}^{6} M_{im}};\quad recall = \frac{1}{6}\sum_{m=1}^{6}\frac{M_{mm}}{\sum_{j=1}^{6} M_{mj}};\quad F_1 = \frac{2\cdot recall\cdot precision}{recall + precision}. \tag{20a,b,c,d}$$

Fig. 7(a) assesses the numbers of accurate and inaccurate predictions for each class. The total number of examples used in the cross-validation is 20,497. The accuracy and F1 score for the neural network model in predictions are respectively 91.39% and 83.09%. It can be seen from Fig. 7(a) that the prediction accuracy in class 5 is the lowest. This is because class 5 corresponds with chaotic vibration that occurs without clear delineation among other parametric combinations, such as those class 5 data points shown in Fig. 6(b). Fig. 7 (b) shows the classification results predicted by the predictor model by changing the periodic impulse frequency and impulse magnitude for the magnet gap 20.55 mm and damping 0.01 N·s/m. Comparing with Fig. 6(b), the surrogate model accurately reproduces the demarcation among dynamic regimes and estimates the dominant frequency ratio at the given input features. In addition, the surrogate model correctly captures the influences of the impulse direction on generating snap-through vibrations. As shown in Fig. 7(b), the periodic impulse in the negative direction realizes snap-through vibrations at a lower periodic impulse frequency around 12 Hz.

From the investigations above, the surrogate model can effectively characterize the dynamics of the nonlinear energy harvesting system. Yet, the criterion and the influence of each design parameter in generating intrawell or snap-through vibration are still implicit in the neural network model. Therefore, in the following section, more insights on selecting design parameters are derived from the trained neural network to assist in determining the optimal strategies for deploying the nonlinear energy harvesting system.

4.2. Optimal strategies from the machine learning model for nonlinear energy harvesting systems

To examine the optimal strategies for maximizing DC power delivery, in this section, the design criteria for realizing the snap-through regime are explicitly described based on the surrogate model. For the sake of robustness of harvester designs, sensitivity is then proposed to quantitively measure the influence of the input design parameters on the output dynamics. Moreover, since the properties of the harvesting circuit affect the harvesting energy efficiency, an impedance-based method is also established based on the predicted classification results to estimate the optimal working load for the harvesting circuit.

4.2.1. Design criteria for maximum performance and robustness of nonlinear energy harvesters

For the nonlinear energy harvester design, snap-through vibrations are preferred for the high energy output for delivery to a storage battery or electrical load. As shown in Fig. 6(b), nonlinear energy harvesters require proper parameter combinations to trigger and sustain large amplitude snap-through vibration. An improper design may inhibit continuous snap-through vibration and result in small

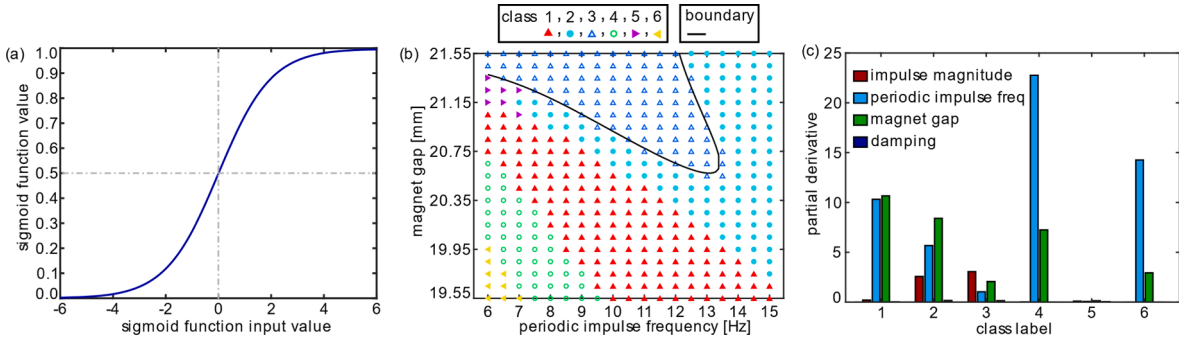

Fig. 8. (a) Plot of sigmoid function. (b) Classification results for damping constant 0.01 N.s/m and impulse −0.1 m/s as functions of the periodic impulse frequency and magnet gap. Classes 1, 2, 4, and 6 respectively represent intrawell vibration with dominant frequency ratio two, one, three, and four, class 3 represents snap-through vibration with dominant frequency ratio one, and class 5 represents chaotic vibration. (c) Partial derivative of each class regrading to input features.

amplitude intrawell vibrations that do not meet the power requirement for electrical loads. Since the surrogate model predicts the classes associated with the vibration type, in this section the critical values of the design parameters are identified through the decision boundary to help efficiently examine the mechanisms that result in high amplitude snap-through vibrations. In addition, a sensitivity analysis is conducted to determine the integrity of the response boundaries against design uncertainties and inconsistent excitations.

As explained in Section 4.1.1, the output of the neural network estimates the possibility of the input features $\boldsymbol{x}$ in class k. The class associated with the highest possibility is the predicted class label for the input features $\boldsymbol{x}$. As such, as long as the predicted possibility for class k is higher than 0.5, the input features $\boldsymbol{x}$ are classified in class k. Since the sigmoid function in Fig. 8(a) is utilized as the activation function, the predicted possibility of 0.5 corresponds to an input of zero. Therefore, the input of zero is taken as the boundary among dynamic regimes [26]. Based on the forward propagation in Eq. (16 a-d), Eq. (21) is employed to determine the critical values of the design parameters for each dynamic regime.

$$\boldsymbol{\Theta}^{(2)}\boldsymbol{b}^{(2)} = 0 \tag{21}$$

For the given problem, there are a total of 6 classes. Class 3 corresponds to the snap-through vibration with dominant frequency ratio one. Therefore, the third equation derived from Eq. (21) corresponds to the critical design parameters to generate snap-through vibrations. Fig. 8(b) demonstrates the predicted classification results for damping constant 0.01 N.s/m and impulse −0.1 m/s as functions of the periodic impulse frequency and magnet gap. The nonlinear boundary between the snap-through and intrawell dynamic regimes is accurately characterized by the nonlinear equation in Eq. (21). As such, the critical need in creating effective tools for bistable harvester design has been addressed. With the criteria determined by Eq. (21), the proper design regarding required excitation and system characteristics is identified for maximizing the harvester performance by demarcating sustainable high energy oscillation. Comparing with simulation individually, the established criteria in Eq. (21) offer a significant improvement for system designs in terms of conciseness and efficiency. In the following investigations, the mechanism for the transfer of dynamics is further discussed with sensitivity analysis.

In addition, for the sake of robust designs, the sensitivity analysis is employed to examine the influential design parameters for each dynamic regime. In the following investigations, the partial derivative is defined as sensitivity to measure the influences of the input parameter on the output classes [5]. To determine the partial derivatives, a small perturbation ε is introduced to one input feature x_j to construct a new feature $\widetilde{x}_j$. Here, the input featurex_j is a normalized value representing the j-th feature of $\boldsymbol{x}$ in Eq. (14), and $\widetilde{x}_j = x_j + \varepsilon$. The new input feature $\widetilde{x}_j$ combining with the rest unchanged features constructs a new feature vector $\widetilde{\boldsymbol{x}}$. The change on output induced by the perturbation ε to x_j^i is termed as Δ_k, and $\Delta_k = (h_{\boldsymbol{\Theta}}(\widetilde{\boldsymbol{x}}))_k - (h_{\boldsymbol{\Theta}}(\boldsymbol{x}))_k$. Therefore, the partial derivative of output $(h_{\boldsymbol{\Theta}}(\boldsymbol{x}))_k$ in regard to the input feature x_j is determined by the Eq. (22a). For N validation examples, the average of partial derivatives defined in Eq. (22b) is taken as the sensitivity of the output classes regarding to the input feature.

$$\widehat{c}_{kj} = \frac{\partial (h_{\boldsymbol{\Theta}}(\boldsymbol{x}))_k}{\partial x_j} = \frac{\Delta_k}{\varepsilon};\ c_{kj} = \frac{1}{N}\sum_{i=1}^{N}\left|\widehat{c}_{kj}^{\,i}\right| \tag{22a, b}$$

As such, the most important or influential input parameter for each output may have the highest c value.

Fig. 8(c) presents the sensitivity results for the classes associated with the four input features. According to Fig. 8(c), the damping constant has the smallest influence on the classification results. For the classes corresponding to intrawell vibrations, namely classes 1, 2, 4, and 6, the periodic impulse frequency and the magnet gap are the two influential factors. As shown in Fig. 8(b), the vibrations associated with class 4 and 6 can only be generated in a narrower frequency range. This indicates it is more important to select the periodic impulse frequency to ensure the generation of the vibrations in classes 4 and 6. In comparison, the intrawell vibrations in class 1 can be achieved in almost the whole range of the periodic impulse frequency and magnet gap. The sensitivities that measure the influence of the periodic impulse frequency and the magnet gap for class 1 are around a similar scale in Fig. 8(c).

Moreover, since the generation of snap-through vibrations requires enough energy to overcome the potential energy barrier, the impulse magnitude is the most influential factor for the snap-through vibration represented by class 3 in Fig. 8(c). If the impulse magnitude is not large enough, the systems may result in intrawell vibrations in class 2. Therefore, the impulse magnitude is a more essential factor in generating intrawell vibration in class 2 comparing with other intrawell classes. In addition, because of the non-resonant nature of the snap-through vibration, the periodic impulse frequency has minor effect on the generation of the snap-through vibration comparing with intrawell vibrations. In terms of the chaotic vibration in class 5, it may be randomly located without evident influential tendency regarding to the design parameters given the results shown in Fig. 6(b) and 7(b). Thus, the chaotic vibration is not sensitive to the changes of input parameters as shown in Fig. 8(c).

Based on the investigations above, the surrogate model established in Section 4.1 is an effective and efficient approach in determining the critical values and sensitivity of design parameters in realizing dynamic regimes. As such, the proper combination of design parameters can be identified to trigger and sustain large amplitude snap-through vibrations.

4.2.2. An impedance-based method for optimal DC power delivery

For energy harvesting systems, the impedance matching, or resistance matching theory is usually employed to ensure the optimal power delivery. Studies have concluded the response frequency is more influential in identifying the optimal working load when the energy harvesting system is under harmonic excitation [3,4,22]. According to the discussions in Section 2.2, the periodic impulse induced responses present similarities with the responses under harmonic excitation. Therefore, in this section, an impedance-based approach is proposed to utilize the dominant frequency component predicted by the surrogate model to help determine the optimal

working load for all combinations of design parameters.

Since the responses under periodic impulse excitation present a single-frequency dominant characterization as discussed in Section 2.2, the mechanical–electrical analogy can be extended to energy harvesting systems under periodic impulse excitations. The dominant frequency in responses is provided by the classification results from the surrogate model. Fig. 9 shows the equivalent circuit of the nonlinear energy harvesting system in Fig. 1(a). In Fig. 9, the transformer turn ratio relates to the electromechanical coupling constant α. The inductance L, resistance R_d, and capacitance C in the circuit respectively relate to the mass $L = m$, viscous damping $R_d = c$, and compliance $C_{s1} = 1/k_1$. A general impedance NL block in Fig. 9 is to characterize the nonlinear effect induced by the nonlinear stiffness k_3 and magnetic force F_{21}. The study [3,4] found that the NL block is analogous to a capacitor that has a response-dependent capacitance value. The current through the circuit before the transformer corresponds to the beam tip velocity via $i = \dot{x}_L$. Because of the ideal impulse assumption, the periodic impulse excitation can be represented by the current i through the circuit, which may experience a sudden change in value at the moment that the impulse is applied.

Since the responses of the nonlinear system under periodic impulse excitation generally can be represented by a single frequency as discussed in Section 2, the source and load impedance can be written as Eq. (23) with the dominant frequency component estimated from the surrogate model in Section 4.1. Here the electrical components inside the red-dashed rectangular in Fig. 4 are termed as source impedance, correspondingly, the harvesting circuit and the beam internal capacitor in the blue-dashed rectangular are together taken as load impedance.

$$R_L = \frac{\mathrm{A}}{\alpha\,\omega_d};\ X_L = \frac{-\mathrm{B}}{\alpha\,\omega_d};\ R_s = \frac{c}{\alpha^2};\ X_s = f(x_L, \omega_d) \tag{23a,b,c,d}$$

where R_L, X_L, R_s, X_s, are respectively the load resistance, load reactance, source resistance, and source reactance; ω_d is the dominant frequency component in the response, which is predicted by the established surrogate model in Section 4.1; A and B identify the characteristic parameters of the standard rectification circuit, which are defined in Eq. (24). Because of the existence of the nonlinear block NL, the source reactance depends on the amplitude x_L and frequency ω_d of the response, which is represented by a general function f. A more detailed analysis of the load and source impedance can be found in reference [3,4].

$$\mathrm{A} = \frac{\alpha\, sin^2\Theta}{C_p\,\pi};\ \mathrm{B} = \frac{\alpha(2\Theta - sin2\Theta)}{2\pi\, C_p};\ \Theta = arccos\left(\frac{\pi - 2\omega_d R\, C_p}{\pi + 2\omega_d R\, C_p}\right) \tag{24a,b,c}$$

The study [3,4] revealed that when $R_S > 2R_L$, the resistance becomes a more influential factor towards the optimal conditions of the harvesting circuit than the reactance. The condition $R_S > 2R_L$ is usually the case given the fact that the electromechanical coupling α is a small value. Therefore, with the dominant frequency component ω_d, the approach to match the load resistance with the source resistance is employed to optimize the delivered power. According to the definition of resistance in Eq. (23), the source resistance is determined by the electromechanical coupling and viscous damping. Therefore, the optimal resistance R can be determined by minimizing the difference between R_S and R_L.

$$R_o = \underset{R}{argmin}(|R_L - R_S|) \tag{25}$$

Fig. 10(a) shows the optimal resistance for the nonlinear harvesting circuit as a function of the periodic impulse frequency for impulse −0.058 m/s, magnet gap 21 mm, and damping constant 0.01 N.s/m. The red circle data labeled simulation are calculated by sweeping through a range of resistances with simulations. Instead, the green triangles named prediction are from the resistance matching approach based on Eq. (25). As shown in Fig. 2(c), when the periodic impulse frequency is around 8 Hz, the numerical response is indeed characterized by multiple frequencies. Yet, based on the definition of the dominant frequency in Section 2.2, the classification results from the surrogate model only considers the influence of the single frequency component. Since the optimal resistance depends on the frequencies of response, there is a disagreement on the predicted optimal resistance around 8 Hz.

In addition, depending on the system parameters and initial conditions, there is a coexistence of snap-through and intrawell vibrations under certain excitation conditions for a nonlinear system. For example, as shown in Fig. 10(b), when the periodic impulse frequency is 10.75 Hz, both snap-through and intrawell vibrations can be introduced by changing the resistance. In this case, the optimal resistance corresponds to the one that can introduce snap-through vibration [18]. Since the surrogate model in Section 4.1 assumes the resistance as a constant to characterize the dynamic regimes of the nonlinear energy harvesting system, the transition from intrawell vibration to snap-through vibration by changing resistance is not included. The impedance analysis based on the classification results from the surrogate model may not be consistent with the values from simulations that consider the transition of vibration types, such as cases at frequencies 10.75 Hz and 12 Hz in Fig. 10(a).

Overall, the prediction results give good approximations of the optimal resistances. Except for the small group of resistances that are associated with co-existent intrawell and snap-through oscillations, the maximum relative error of 'prediction' comparing with

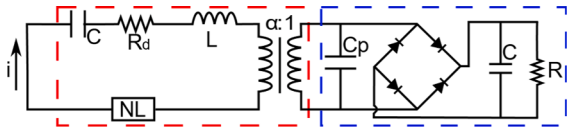

Fig. 9. Equivalent circuit of a nonlinear energy harvesting system with impulse excitation.

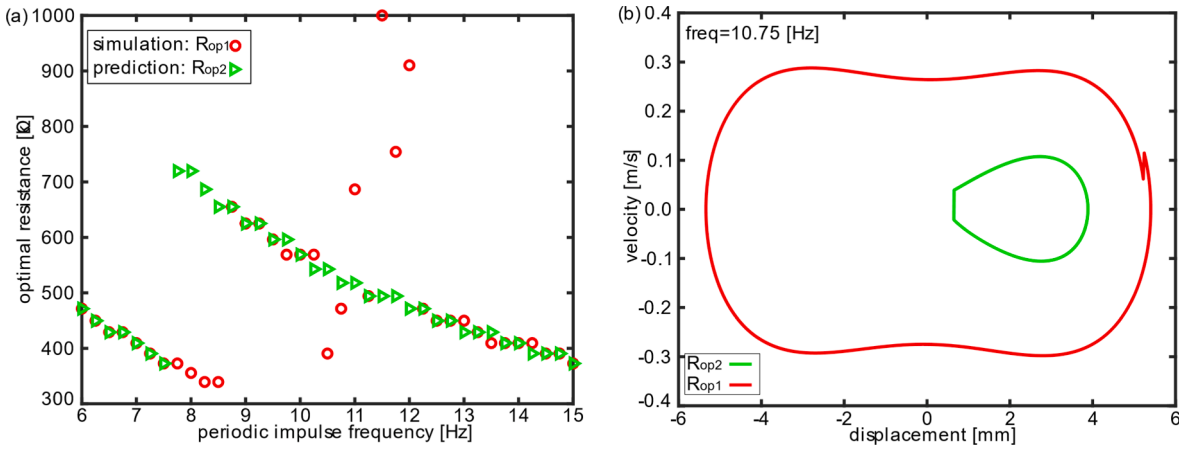

Fig. 10. (a) Optimal resistances across excitation frequencies. (b) Phase portraits with two optimal resistances at periodic impulse frequency 10.75 Hz.

simulation is less than 5%. It is reasonable to employ the simple resistance matching approach to approximate optimal resistances for the harvesting circuit.

With the emerging implementation of vibration energy harvesting systems to support the Internet-of-Things devices, significant operational data may be collected in the field. A synthesis of first-principles models and machine learning algorithms can provide real-time optimization of the energy harvesting platforms to ensure sustainable operation of power delivery. This research demonstrates one such synthesis by establishing a surrogate model to efficiently identify the mechanical and electrical mechanisms for maximizing DC power delivery. Here, the four system parameters (impulse magnitude I, periodic impulse frequency f_{exc}, magnet gap H, and damping constant c) are selected as an example to validate the effectiveness of the created surrogate model. Nevertheless, the proposed synthesis algorithm can be applied to incorporate a greater number and greater range of system parameters, such as beam shape parameters, piezoelectrical material characteristics, magnetic field changes, and more. With the anticipated progress in this emerging field, the proposed surrogate model may be a powerful tool to analyze piezo-electro-mechanical dynamic behavior of nonlinear energy harvesting systems subjected to periodic impulse excitation.

5. Conclusion

This research integrates machine learning algorithms with the physical insights of a first-principles model to examine strategies to ensure nonlinear energy harvesting systems that are subjected to periodic impulse excitation deliver peak electrical power to loads. The investigations indicate that the direction of the periodic impulse plays a significant factor for electrical power generation, due to the asymmetry of system energy associated with the nonlinearities. A predictor model is created through a neural network analysis of simulation data to identify design and excitation parameter regimes that ensure high amplitude snap-through dynamics are induced, providing best DC current delivery. The accuracy of the predictions are confirmed through experiments and against cross-validation simulation data. The demarcation of parameters that result in snap-through are then probed through a first-principles model to confirm that optimal circuit design conditions, specifically the resistance, suggested by the predictor model agree with the principle of impedance matching. This research demonstrates a successful synthesis of machine learning algorithms and first principles models to guide attention to optimal designs of nonlinear energy harvesting systems subjected to periodic impulse excitation.

Declaration of Competing Interest

The authors declare that they have no known competing financial interests or personal relationships that could have appeared to influence the work reported in this paper.

Acknowledgments

This research is supported in part by the National Science Foundation (Award No. 1661572), by the National Science Foundation Faculty Early Career Development Award (No. 2054970), and by The Ohio State University Presidential Fellowship. The authors are grateful to Mide Technology for hardware support.

References

[1] E. Alpaydin, Introduction to Machine Learning, 3rd ed., The MIT Press, 2014.
[2] S.L. Brunton, J.L. Proctor, J.N. Kutz, Discovering governing equations from data by sparse identification of nonlinear dynamical systems, Proc. Natl. Acad. Sci. 113 (15) (2016) 3932–3937.

[3] W. Cai, R.L. Harne, Electrical power management and optimization with nonlinear energy harvesting structures, J. Intell. Mater. Syst. Struct. 30 (2) (2019) 213–227.
[4] W. Cai, R.L. Harne, Vibration energy harvesters with optimized geometry, design, and nonlinearity for robust direct current power delivery, Smart Mater. Struct. 28 (7) (2019) 075040, https://doi.org/10.1088/1361-665X/ab2549.
[5] Cao, M., Alkayem, N., Pan, L., & Novak, D. (2016). Advanced methods in neural networks-based sensitivity analysis with their applications in civil engineering. Artificial neural networks: models and applications, Rijeka, Croatia, IntechOpen, 335-353.
[6] Chen, G., Zuo, Y., & Sun, J. (2012). Support-vector-machine-based reduced-order model for limit cycle oscillation prediction of nonlinear aeroelastic system. Mathematical problems in engineering, 2012.
[7] S. Chiacchiari, F. Romeo, D.M. McFarland, L.A. Bergman, A.F. Vakakis, Vibration energy harvesting from impulsive excitations via a bistable nonlinear attachment, Int. J. Non Linear Mech. 94 (2017) 84–97.
[8] F. Cottone, H. Vocca, L. Gammaitoni, Nonlinear energy harvesting, Phys. Rev. Lett. 102 (8) (2009), 080601.
[9] Q. Dai, R.L. Harne, Charging power optimization for nonlinear vibration energy harvesting systems subjected to arbitrary, persistent base excitations, Smart Mater. Struct. 27 (1) (2018) 015011, https://doi.org/10.1088/1361-665X/aa9a13.
[10] Q. Dai, I. Park, R.L. Harne, Impulsive energy conversion with magnetically coupled nonlinear energy harvesting systems, J. Intell. Mater. Syst. Struct. 29 (11) (2018) 2374–2391.
[11] A. Erturk, D. Inman, Piezoelectric Energy Harvesting, John Wiley & Sons, Chichester, 2011.
[12] S. Fang, X. Fu, W.-H. Liao, Asymmetric plucking bistable energy harvester: Modeling and experimental validation, J. Sound Vib. 459 (2019) 114852, https://doi.org/10.1016/j.jsv.2019.114852.
[13] M. Ferrari, V. Ferrari, M. Guizzetti, B. Andò, S. Baglio, C. Trigona, Improved energy harvesting from wideband vibrations by nonlinear piezoelectric converters, Sens. Actuat. A 162 (2) (2010) 425–431.
[14] X. Fu, W.-H. Liao, Nondimensional model and parametric studies of impact piezoelectric energy harvesting with dissipation, J. Sound Vib. 429 (2018) 78–95.
[15] A. Hande, R. Bridgelall, B. Zoghi, Vibration energy harvesting for disaster asset monitoring using active RFID tags, Proc. IEEE 98 (9) (2010) 1620–1628.
[16] R.L. Harne, K.W. Wang, A review of the recent research on vibration energy harvesting via bistable systems, Smart Mater. Struct. 22 (2) (2013) 023001, https://doi.org/10.1088/0964-1726/22/2/023001.
[17] R.L. Harne, M. Thota, K.W. Wang, Concise and high-fidelity predictive criteria for maximizing performance and robustness of bistable energy harvesters, Appl. Phys. Lett. 102 (5) (2013) 053903, https://doi.org/10.1063/1.4790381.
[18] R.L. Harne, C. Zhang, B. Li, K.W. Wang, An analytical approach for predicting the energy capture and conversion by impulsively-excited bistable vibration energy harvesters, J. Sound Vib. 373 (2016) 205–222.
[19] T. Huguet, M. Lallart, A. Badel, Bistable vibration energy harvester and SECE circuit: exploring their mutual influence, Nonlinear Dyn. 97 (1) (2019) 485–501.
[20] Karpatne, A., Watkins, W., Read, J., & Kumar, V. (2017). Physics-guided neural networks (pgnn): An application in lake temperature modeling. arXiv preprint arXiv, 1710, 11431.
[21] S. Leadenham, A. Erturk, Mechanically and electrically nonlinear non-ideal piezoelectric energy harvesting framework with experimental validations, Nonlinear Dyn. 99 (1) (2020) 625–641.
[22] Liang, J., & Liao, W. (2011). Impedance modeling and analysis for piezoelectric energy harvesting systems. IEEE/ASME Transactions on Mechatronics, 17(6), 1145-1157. Retrieved from Impedance modeling and analysis for piezoelectric energy harvesting systems.
[23] J. Ling, R. Jones, J. Templeton, Machine learning strategies for systems with invariance properties, J. Comput. Phys. 318 (2016) 22–35.
[24] Mahanta, J. (2017, July). Retrieved from Introduction to Neural Networks, Advantages and Applications: https://towardsdatascience.com/introduction-to-neural-networks-advantages-and-applications-96851bd1a207.
[25] D. Mallick, A. Amann, S. Roy, Surfing the high energy output branch of nonlinear energy harvesters, Phys. Rev. Lett. 117 (19) (2016), 197701.
[26] Mishra, M. (2018, June). Retrieved from CLASSIFICATION: An important concept in Machine Learning: https://towardsdatascience.com/classification-an-important-concept-in-machine-learning-af6ff4cb2cfd.
[27] L. Moro, D. Benasciutti, Harvested power and sensitivity analysis of vibrating shoe-mounted piezoelectric cantilevers, Smart Mater. Struct. 19 (11) (2010) 115011, https://doi.org/10.1088/0964-1726/19/11/115011.
[28] D. Quinn, A. Triplett, A. Vakakis, L. Bergman, Energy harvesting from impulsive loads using intentional essential nonlinearities, J. Vib. Acoust. 133 (1) (2011).
[29] Reindl, L. (2018). Retrieved from Power supply for wireless sensor systems: http://www.sensornets.org/Documents/Previous_Invited_Speakers/2018/SENSORNETS2018_Reindl.pdf.
[30] K. Remick, H.K. Joo, D.M. McFarland, T.P. Sapsis, L. Bergman, D.D. Quinn, A. Vakakis, Sustained high-frequency energy harvesting through a strongly nonlinear electromechanical system under single and repeated impulsive excitations, J. Sound Vib. 333 (14) (2014) 3214–3235.
[31] X. Rui, Y.u. Zhang, Z. Zeng, G. Yue, X. Huang, J. Li, Design and analysis of a broadband three-beam impact piezoelectric energy harvester for low-frequency rotational motion, Mech. Syst. Sig. Process. 149 (2021) 107307, https://doi.org/10.1016/j.ymssp.2020.107307.
[32] C. Vasques, R. Moreira, J. Rodrigues, Viscoelastic damping technologies-Part I: modeling and finite element implementation, J. Adv. Res. Mech. Eng. 1 (2) (2010).
[33] N. Wagner, J. Rondinelli, Theory-guided machine learning in materials science, Front. Mater. 3 (2016) 28.
[34] J. Wang, W.-H. Liao, Attaining the high-energy orbit of nonlinear energy harvesters by load perturbation, Energy Convers. Manage. 192 (2019) 30–36.
[35] J. Wang, D. Sun, S. Liu, X. Zhang, Damping characteristics of viscoelastic damping structure under coupled condition, Mathematical and Computational Applications 22 (1) (2017) 27.
[36] J. Wang, B. Zhao, W.-H. Liao, J. Liang, New insight into piezoelectric energy harvesting with mechanical and electrical nonlinearities, Smart Mater. Struct. 29 (4) (2020) 04LT01, https://doi.org/10.1088/1361-665X/ab7543.
[37] Willard, J., Jia, X., & Xu, S. (2020). Integrating physics-based modeling with machine learning: A survey. arXiv preprint arXiv:2003, 04919.
[38] Y. Wu, A. Badel, F. Formosa, W. Liu, A. Agbossou, Nonlinear vibration energy harvesting device integrating mechanical stoppers used as synchronous mechanical switches, J. Intell. Mater. Syst. Struct. 25 (14) (2014) 1658–1663.
[39] Z. Xiao, T.Q. Yang, Y. Dong, X.C. Wang, Energy harvester array using piezoelectric circular diaphragm for broadband vibration, Appl. Phys. Lett. 104 (22) (2014) 223904, https://doi.org/10.1063/1.4878537.
[40] K. Ylli, D. Hoffmann, A. Willmann, P. Becker, B. Folkmer, Y. Manoli, Energy harvesting from human motion: exploiting swing and shock excitations, Smart Mater. Struct. 24 (2) (2015) 025029, https://doi.org/10.1088/0964-1726/24/2/025029.
[41] Y. Yu, H. Yao, Y. Liu, Structural dynamics simulation using a novel physics-guided machine learning method, Eng. Appl. Artif. Intell. 96 (2020) 103947, https://doi.org/10.1016/j.engappai.2020.103947.
[42] S. Zeadally, F.K. Shaikh, A. Talpur, Q.Z. Sheng, Design architectures for energy harvesting in the Internet of Things, Renew. Sustain. Energy Rev. 128 (2020) 109901, https://doi.org/10.1016/j.rser.2020.109901.
[43] C. Zhang, R.L. Harne, B. Li, K.W. Wang, Reconstructing the transient, dissipative dynamics of a bistable Duffing oscillator with an enhanced averaging method and Jacobian elliptic functions, Int. J. Non Linear Mech. 79 (2016) 26–37.
[44] Z. Zhang, C. Sun, Structural damage identification via physics-guided machine learning: a methodology integrating pattern recognition with finite element model updating, Struct. Health Monitor. 20 (4) (2021) 1675–1688.
[45] S. Zhou, J. Cao, D.J. Inman, S. Liu, W. Wang, J. Lin, Impact-induced high-energy orbits of nonlinear energy harvesters, Appl. Phys. Lett. 106 (9) (2015) 093901, https://doi.org/10.1063/1.4913606.
[46] Z. Zhou, W. Qin, W. Du, P. Zhu, Q.i. Liu, Improving energy harvesting from random excitation by nonlinear flexible bi-stable energy harvester with a variable potential energy function, Mech. Syst. Sig. Process. 115 (2019) 162–172.